applied sciences

MDPI

Article

Three Dimensional Lifetime-Multiplex Tomography Based on Time-Gated Capturing of Near-Infrared Fluorescence Images

Masakazu Umezawa *, Keiji Miyata, Kyohei Okubo and Kohei Soga *

Department of Materials Science and Technology, Faculty of Advanced Engineering, Tokyo University of Science, 6-3-1 Niijuku, Katsushika, Tokyo 125-8585, Japan; kaka1995soccer@outlook.jp (K.M.); kyohei.okubo@rs.tus.ac.jp (K.O.)

* Correspondence: masa-ume@rs.tus.ac.jp (M.U.); mail@ksoga.com (K.S.)

Featured Application: The NIRF-TGI-CT presented in this study is expected to be applied to the acquisition of information, that is, temperature, on the deep interior of samples, especially biological tissues possessing refractive index interfaces in inside that cause light scattering.

Abstract: We report a computed tomography (CT) technique for mapping near-infrared fluorescence (NIRF) lifetime as a multiplex three-dimensional (3D) imaging method, using a conventional NIR camera. This method is achieved by using a time-gated system composed of a pulsed laser and an NIR camera synchronized with a rotatable sample stage for NIRF-CT imaging. The fluorescence lifetimes in microsecond-order of lanthanides were mapped on reconstructed cross-sectional and 3D images, via back-projection of two-dimensional projected images acquired from multiple angles at each time point showing fluorescence decay. A method to select slopes (the observed decay rates in time-gated imaging) used for the lifetime calculation, termed as the slope comparison method, was developed for the accurate calculation of each pixel, resulting in reduction of image acquisition time. Time-gated NIRF-CT provides a novel choice for multiplex 3D observation of deep tissues in biology.

Keywords: time-gated imaging; fluorescence lifetime; near-infrared; rare-earth-doped ceramics; deep tissue imaging; second biological window

Citation: Umezawa, M.; Miyata, K.; Okubo, K.; Soga, K. Three Dimensional Lifetime-Multiplex Tomography Based on Time-Gated Capturing of Near-Infrared Fluorescence Images. *Appl. Sci.* **2022**, *12*, 7721. https://doi.org/10.3390/app12157721

Academic Editor: Paolo Prosposito

Received: 12 May 2022
Accepted: 29 July 2022
Published: 31 July 2022

1. Introduction

Three-dimensional (3D) functional imaging of targets in deep live tissues is a fundamental challenge in biophotonics. For the functional imaging of deep tissues, X-ray projection and computed tomography (CT) [1], ultrasonography [2,3], positron-emission tomography (PET), and magnetic resonance imaging (MRI) [4] are useful techniques in biomedical fields. However, each technique has some limitations, such as ionizing radiation exposure of X-rays, low spatial resolution in PET and ultrasound, and the need for complex equipment for MRI. Near-infrared (NIR) imaging is an additional method for observing deep biological tissues. For example, indocyanine green (ICG), the working wavelength which is called NIR-I (700−950 nm), is used to visualize blood flow and liver function for surgical guidance [5]. NIR wavelengths longer than 1000 nm, over-thousand-nanometer (OTN) NIR, also called NIR-II and NIR-III [6], have the advantages of minimizing scattering by biological tissues [7] and, thus, expanding the observation depth to 1–2 cm [8], as compared to several millimeters in the NIR wavelength of ICG. Thus, optical imaging in the NIR wavelength range, especially OTN-NIR, enables observation of biological deep tissues transparently [9]. Recently, the distinction of submucosal tumors through the mucosal layer using spectral features in NIR images has also been reported [10]. For detection, cameras for visible and NIR-I light should be replaced with cameras with indium gallium arsenide (InGaAs) sensitive to OTN-NIR [6]. Nevertheless, in this wavelength range, fluorescence imaging of deep tissues can be performed using a simple device composed of a laser light source for excitation, optical mirrors and filters, and cameras.

We aimed to perform 3D mapping of NIR phosphors with multiplexity based on the fluorescence lifetime, which corresponds to the decay rate of emission. Tomography of the decay rate of signals from inside the tissues is established in the imaging of the nuclear spin relaxation under a controlled magnetic field for MRI. Instead of nuclear spin relaxation, the decay rate of optical emission is used for tomographic imaging. The decay rate of the emitted light from phosphors provides the fluorescence lifetime, which is a time constant independent of the absolute fluorescence intensity or power density of the laser for excitation. Actually, fluorescence lifetime has attracted attention for realizing multiplex imaging in the OTN-NIR wavelength range [11]. In microscopic imaging, 3D mapping of fluorescence lifetimes using fluorescence lifetime imaging microscopy (FLIM) with a single-plane illumination (recently named light-sheet) setup [12,13], or with a confocal system [14], has been reported. A methodology for fluorescence lifetime tomography has also been proposed [15] and experimentally validated by microscopic tomography using FLIM 3D fluorescence lifetime imaging using high-speed cameras [16–18].

The NIR fluorescence (NIRF) lifetime images can be captured by a time-gated imaging (TGI) system. It is composed of a synchronized image acquisition system with a conventional NIR camera, and a pulsed laser for excitation to collect the decay images of fluorescence immediately (at several tens of microseconds) after cutting off the laser [19]. Contrasting the fluorescence lifetime also reduces noise, such as autofluorescence in fluorescence imaging in the ultraviolet, visible [20], and NIR wavelength ranges [21,22]. Multiplexity also realizes contactless temperature imaging of deep tissues using $NaYF_4$ co-doped with Nd^{3+} and Yb^{3+} [23]. Because NIR fluorescence makes deep tissues observable, its cross-sectional images can be obtained from two-dimensional projected images acquired from various angles by reconstruction with CT, based on the back-projection algorithm [24–26]. Although volumetric optical tomography using fluorescence has been reported since 2005 [24], the greatest advantage of using OTN-NIR light is expanding the observation depth to the order of organs and the whole body of small animals. The objective of this study is to develop a lifetime-based multiplex 3D imaging method for NIRF in deep tissues, by synchronizing the TGI system using a conventional NIR camera, with a rotatable stage for controlling the detection angles.

2. Materials and Methods

2.1. Materials

$Nd(NO_3)_3{\cdot}6H_2O$ and $Yb(NO_3)_3{\cdot}6H_2O$ were purchased from Sigma-Aldrich Co. (St. Louis, MO, USA). $Y(NO_3)_3{\cdot}6H_2O$ and NaF were purchased from Kanto Chemical Co. Inc. (Tokyo, Japan). NH_4F and $NH_4H_2PO_4$ were purchased from Fujifilm Wako Pure Chemical Co. (Osaka, Japan). All reagents were used without further purification.

2.2. Synthesis of Nd^{3+}- and Yb^{3+}-Doped $NaYF_4$

$NaYF_4$ co-doped with Nd^{3+} and Yb^{3+} ($NaYF_4$: Nd^{3+}, Yb^{3+}) was synthesized using the standard co-precipitation method [27]. $Y(NO_3)_3{\cdot}6H_2O$ (6.0 mmol), $Nd(NO_3)_3{\cdot}6H_2O$ (3.0 mmol), and $Yb(NO_3)_3{\cdot}6H_2O$ (1.0 mmol) were dissolved in 10 mL of distilled water. The mixture solution was dropped into 40 mL of an aqueous solution of NaF (60 mmol) and stirred for 1 h at 75 °C. After stirring, the precipitate was collected by centrifugation (20,000× g, 10 min, ×3). The samples were then dried at 80 °C for 24 h. Subsequently, the samples were treated with NH_4F (800 mg) for 1 h at 550 °C to yield $NaYF_4$ co-doped with 30 mol% Nd^{3+} and 10 mol% Yb^{3+}.

2.3. Synthesis of Nd^{3+}- and Yb^{3+}-Doped YPO_4

YPO_4 co-doped with Nd^{3+} and Yb^{3+} (YPO_4: Nd^{3+}, Yb^{3+}) was synthesized using the standard solvothermal method [28]. $Y(NO_3)_3{\cdot}6H_2O$ (8.1 mmol), $Nd(NO_3)_3{\cdot}6H_2O$ (4.05 mmol), $Yb(NO_3)_3{\cdot}6H_2O$ (1.35 mmol), and $NH_4H_2PO_4$ (13.5 mmol) were dissolved in 30 mL of distilled water. The mixture solution was stirred for 30 min. After stirring, the particles were encapsulated in a 40 mL Teflon inliner and subjected to a steel autoclave for

6 h at 200 °C, followed by centrifugation (20,000× g, 10 min, ×2) to collect the precipitate. The obtained samples were calcined at 900 °C for 30 min.

2.4. Fluorescence Analysis

The fluorescence spectra of the samples under 808 nm excitation were analyzed using a spectrometer (NIR Quest; Ocean Optics Inc., Dunedin, FL, USA). The fluorescence lifetimes of the samples were analyzed at 25 °C using an optical parametric oscillator (Surelite II-10; Continuum Inc., San Jose, CA, USA) pumped by a frequency-tripled Nd-doped yttrium aluminum garnet laser operating at 355 nm. The optical parametric oscillator provides 5 ns pulses at a wavelength of 808 nm with an average energy of 9.5 mJ and a repetition rate of 10 Hz. The time evolution was detected using an infrared photomultiplier (H10330C; Hamamatsu Photonics Co. Ltd., Shizuoka, Japan) connected to a digital oscilloscope (TDS2024C, Tektronix Inc., Beaverton, OR, USA) with a long-pass filter (#86–248; Edmund Optics Inc., Barrington, NJ, USA) to detect only fluorescence.

2.5. Image Acquisition for Time-Gated Computed Tomography of NIRF

By connecting TGI and a rotatable stage to a personal computer, we simultaneously controlled the pulse generator, NIR camera, and rotatable stage (Figure 1). The sample containing OTN-NIR fluorophores was fixed on the rotatable stage. Instead of the continuous-wave laser used for excitation in conventional fluorescence imaging, a pulse-wave laser was used in the TGI acquisition system. A custom-built pulsed laser diode (wavelength: 808 nm; power: 5 A) was used to generate 1 ms pulses at a repetition rate of 21 Hz. The pulse-to-pulse separation was set to 40 ms. A time series of fluorescence decay images was obtained using an NIR camera (ARTCAM-0016TNIR; Artlay Co., Ltd., Tokyo, Japan). A 980 nm long-pass filter was placed in front of the NIR camera to avoid entering of the excitation light to the camera. In the NIRF-TGI system, the projected images of the fluorescence decay were recorded by controlling the timing between the pulsed laser for excitation and the trigger for image acquisition by NIR camera as a fluorescence detector. A digital delay/pulse generator (DG535; SRS Inc., Sunnyvale, CA, USA) was connected to the laser and the camera to trigger them at a delayed time (t_{delay}). To obtain the fluorescence decay curves, a series of fluorescence images (8-bit) was acquired, where t_{delay} ranged from 0 to 1000 μs in increments of 50 μs. To obtain time-dependent changes in the fluorescence image at each angle, the sample was rotated using the rotatable stage. A total of 720 projected images at each delay time were collected at angular intervals of 0.5°. Time-dependent changes in the fluorescence images were obtained at each angle, whereas the fluorescence tomographic images were reconstructed using CT. A cross-sectional fluorescence image for each delay time was acquired using the back-projection method [26] from two-dimensional projected images acquired at each angle for a certain delay time. The fluorescence lifetime was calculated for each pixel from the obtained tomographic fluorescence images and color-coded according to the value. Tomographic fluorescence lifetime images were stacked using ImageJ to obtain a 3D image.

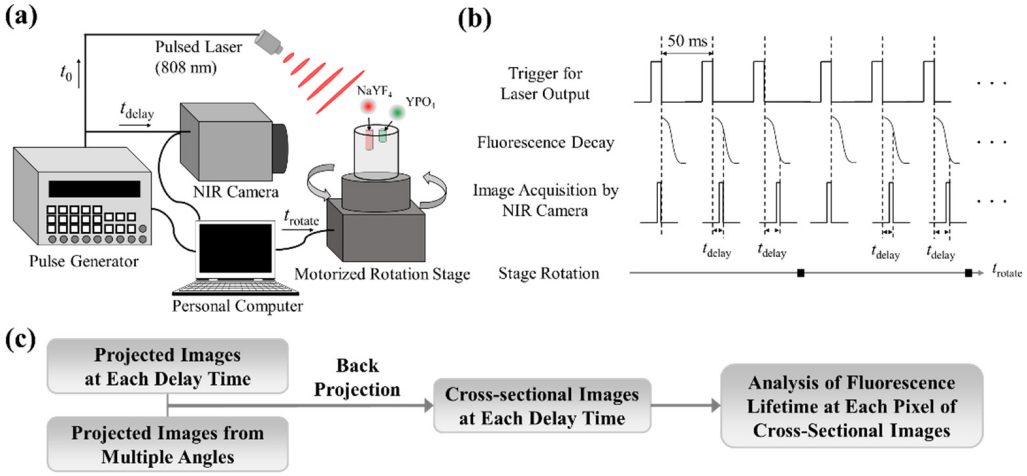

Figure 1. Setup of computed tomography (CT) for near-infrared fluorescence (NIRF) time-gated imaging (TGI). (**a**) Schematic illustration of the system for NIRF-TGI combined with CT. (**b**) Time chart of pulsed irradiation for fluorescence excitation at 808 nm, image acquisition using the NIRF-TGI system and time points when the motorized stage rotates, along with the expected profiles of fluorescence decay. This system can acquire projected images at controlled delay times after turning off the excitation laser to record images of fluorescence decay. The projected images of the fluorescence decay of samples can be collected from multiple angles to control the rotation of the stage. As shown in (**c**) the block diagram of the image acquisition and processing for conducting NIRF-TGI-CT, tomographic images are first reconstructed for each delay time by conventional back-projection. Next, the fluorescence lifetimes can be determined at each pixel of the tomograms obtained at multiple delay times.

3. Results

3.1. Optical Properties of Samples

NIR fluorophores with different fluorescence lifetimes were prepared by doping guest ions into two different hosts with different phonon energies; $NaYF_4$ and YPO_4, and were used as composites by embedding in agar gel. Lanthanide-doped ceramic nanoparticles are used as NIR phosphors because they have the advantage of long lifetimes (several hundred microseconds). This is because of the shielding of 4f electrons by external electrons in the 5s and 5p orbitals for suppressing thermal relaxation, as well as essentially small rates of the optical transition of the 4f electrons with magnetic and forced-electric dipole moment transitions [29]. The guest ions were Nd^{3+} as a sensitizer for 808 nm excitation with the $^4I_{9/2} \rightarrow {}^4F_{5/2}$ transition and Yb^{3+} to emit fluorescence in the 1000–1040 nm wavelength range by the $^2F_{5/2} \rightarrow {}^2F_{7/2}$ transition. As shown in Figure 2a, the targeted fluorescence spectra are well observed for both samples, measured using a spectrometer in the wavelength range of 1000–1040 nm, while both showed their characteristic decay rate (Figure 2b). As shown in the energy level diagram in Figure 2c, minor fluorescence from the Nd^{3+} peaked at 1064 nm by the $^4F_{3/2} \rightarrow {}^4I_{11/2}$ transition is also observed. The fluorescent particles were prepared in sizes so that their fluorescence properties are not affected by anything other than the host material ($NaYF_4$ and YPO_4) [23].

Fluorescence lifetimes vary according to the rates of energy transfer and thermal relaxation of excited photons. For instance, the fluorescence lifetime of $NaYF_4$ nanoparticles co-doped with Nd^{3+} and Yb^{3+} can be controlled by the dopant ion concentrations and used for multiplex imaging of in vivo deep tissues (stomach and liver) [30]. The fluorescence lifetimes of 4f electrons in trivalent lanthanide ions are also controlled by thermal relaxation, called multi-phonon relaxation (MPR), and radiative transition rates. The MPR strongly depends on the phonon energy of the host [29]. The phonon energies of YPO_4 and $NaYF_4$ are 1080 cm^{-1} [31] and 300−400 cm^{-1} [32], respectively. Therefore, the fluorescence lifetime of YPO_4: Nd^{3+}, Yb^{3+} (240 µs) is shorter than that of $NaYF_4$: Nd^{3+}, Yb^{3+} (470 µs) (Figure 2b), as determined by analysis using a synchronized system of a photomultiplier detector and a

pulsed 808 nm laser extracted from an Nd-doped yttrium aluminum garnet laser. Samples of phosphors embedded in agar gel (Figure 2d), a model of tissues containing water, were used for analysis.

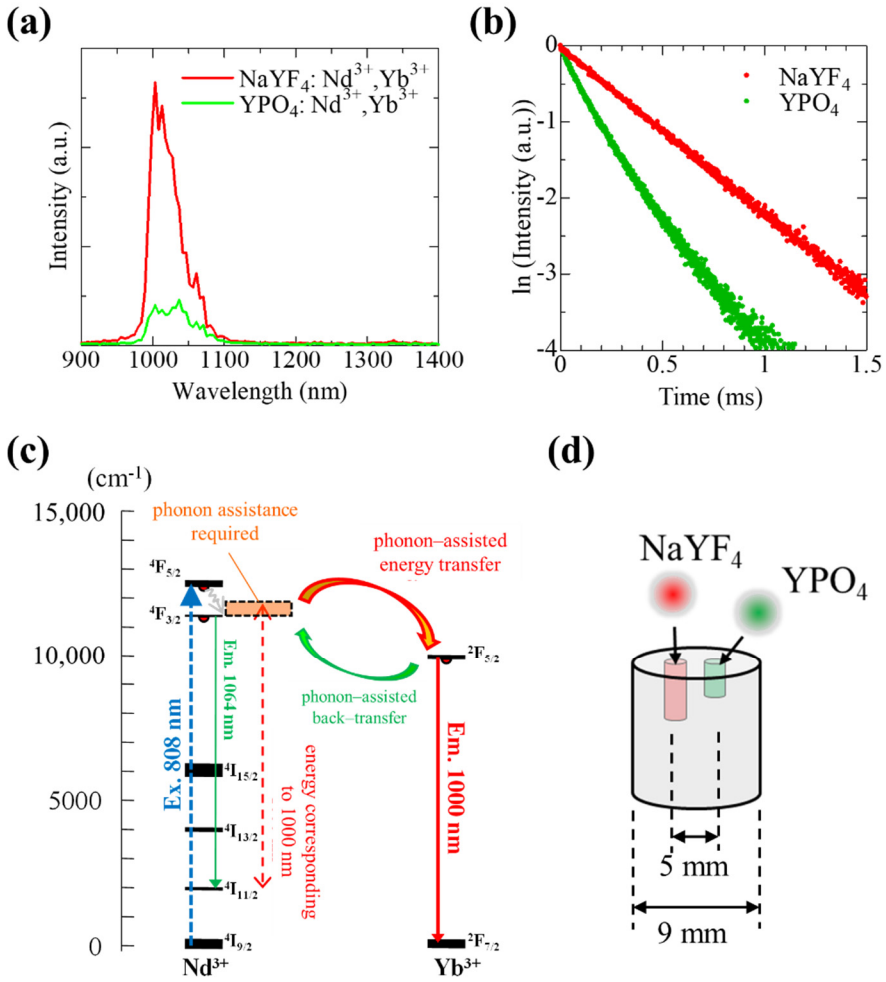

Figure 2. Optical properties of YPO_4 and $NaYF_4$ co-doped with Nd^{3+} and Yb^{3+}. (**a**) Emission spectra of NIRF of Yb^{3+} ($^4F_{5/2} \rightarrow {}^4F_{7/2}$) from $NaYF_4$: Nd^{3+}, Yb^{3+} and YPO_4: Nd^{3+}, Yb^{3+}. (**b**) Fluorescence decay curves of $NaYF_4$: Nd^{3+}, Yb^{3+} (fluorescence lifetime: 470 µs) and YPO_4: Nd^{3+}, Yb^{3+} (240 µs) detected using a photomultiplier tube. (**c**) Energy diagram of ceramic particles co-doped with Nd^{3+} and Yb^{3+}, which was used as the sensitizer excited by an 808 nm laser and as a 1000 nm emitter. (**d**) Schematic illustration of the sample from which the data in Figures 3 and 4 were obtained. $NaYF_4$: Nd^{3+}, Yb^{3+} (470 µs) and YPO_4: Nd^{3+}, Yb^{3+} (240 µs) were embedded in an agar gel as a model of water-containing tissue.

3.2. Computed Tomography of NIRF Detected at Each Delay Time in TGI

Two-dimensional projected NIRF images were collected for the sample containing YPO_4: Nd^{3+}, Yb^{3+} and $NaYF_4$: Nd^{3+}, Yb^{3+} placed on a rotatable stage. The projected images from multiple angles were acquired by synchronizing the movement of the stage rotation and the image acquisition by TGI. This system enables recording of the change in the position of each fluorophore depending on the angle of image acquisition (Figure 3a). In this NIRF-TGI-CT system, the stage with a sample rotates by a set angle after imaging with TGI at an angle of image acquisition. The projected images of the fluorescence decay were also recorded for each angle by delaying the timing of the image acquisition after turning off the laser for excitation (Figure 3b). Using conventional back-projection that is applicable to images showing a fluorescent intensity distribution, the cross-sectional NIRF images of the samples were reconstructed for each delay time (Figure 3c).

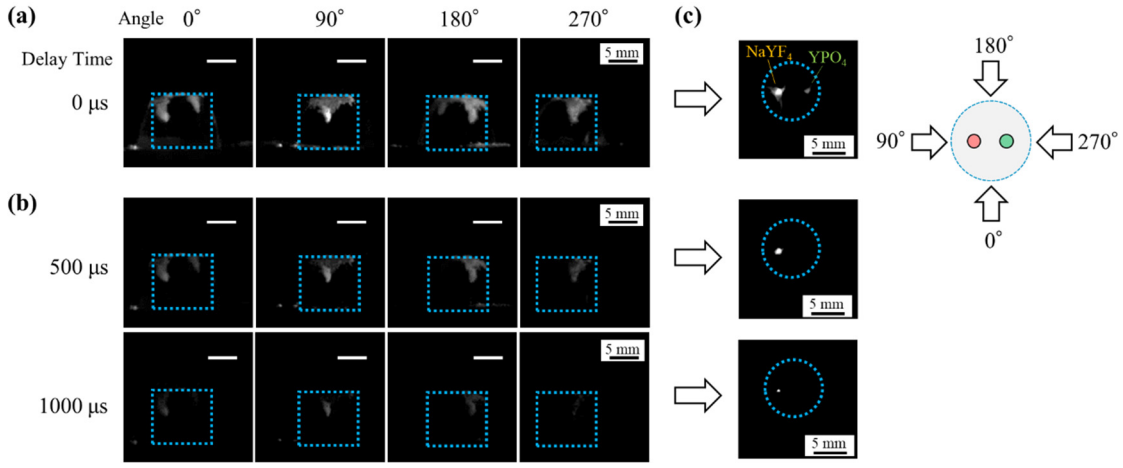

Figure 3. Two-dimensional projected images and reconstructed cross-sectional images of NIR fluorophores recorded by the NIRF-TGI-CT image acquisition system. (**a**) Two-dimensional projected images acquired from each angle at a delay time of 0 μs after turning off the laser for excitation. (**b**) Projected images of the fluorescence decay recorded at an indicated delay time from each angle. Integration: 100 μs. Laser power: 5 W/cm^2. (**c**) Reconstructed cross-sectional images of NIR fluorophores of the sample at each delay time. The dotted blue lines indicate the form of the cylinder-shaped agar gel, which looks rectangular when seen from the side to collect the projected images (**b**), and circular when seen at cross-sections, as shown in (**c**). The red and green in the illustration indicate $NaYF_4$ and YPO_4 co-doped with Nd^{3+} and Yb^{3+}.

3.3. Fluorescence Lifetime Mapping to Cross-Sectional Images

For all cross-sectional fluorescence images (tomograms) taken at each angle and at each delay time, the rate of time-dependent decay was calculated from the fluorescence intensity for each pixel. The fluorescence decay normalized by the initial intensity at a delay time of 0 μs showed different decay rates between the YPO_4 and $NaYF_4$ particles (Figure 4a), of which the positions are shown on the tomogram (Figure 4b). The calculated lifetimes of YPO_4: Nd^{3+}, Yb^{3+} and $NaYF_4$: Nd^{3+}, Yb^{3+} were 296 ± 3 μs and 516 ± 39 μs. Although accuracy of the calculation is still a challenge, the contrast of their fluorescence lifetime was mapped on the cross-sectional images by the NIRF-TGI-CT technique. Stacking these cross-sectional images provides a 3D fluorescence lifetime distribution image that can distinguish phosphors with different fluorescence lifetimes (Video S1).

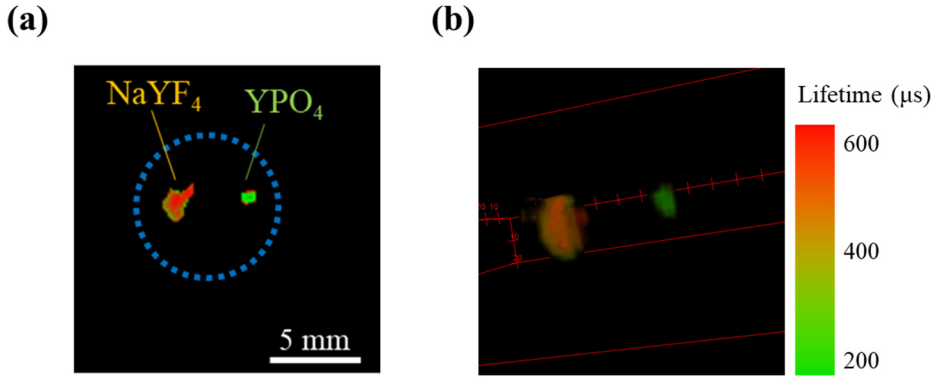

Figure 4. Fluorescence lifetime mapping to cross-sectional and 3D images. (**a**) Cross-sectional images of the fluorescence lifetime difference of $NaYF_4$: Nd^{3+}, Yb^{3+} and YPO_4: Nd^{3+}, Yb^{3+}. Blue dotted lines show the outline of the sample. (**b**) 3D images of the fluorescence lifetimes of $NaYF_4$: Nd^{3+}, Yb^{3+} and YPO_4: Nd^{3+}, Yb^{3+}. 3D images were obtained by stacking the fluorescence lifetime distributions of the cross-sectional images.

3.4. Slope Comparison Method (SCM)—Time-Gated Imaging of Fluorescence Lifetime to Obtain Fluorecence Decay with Minimal Number of Delay-Time Points

Finally, we investigated the NIRF-TGI protocols and methods of fluorescence lifetime calculation to shorten the imaging time of NIRF-TGI-CT. As described in the previous sections, the fluorescence decay was imaged at a total of 21 delay times, 50 µs each from 0 to 1000 µs, after blocking the excitation light for each imaging angle. In other words, the cycle of irradiation of pulsed excitation light and image acquisition was repeated 21 times to obtain one NIRF decay image. A method for accurate observation of the fluorescence decay rate (lifetime) with a smaller number of delay time points is needed to map the lifetime to cross-sectional images in a shorter time. In this study, we propose a new method for fluorescence lifetime calculation called the slope comparison method (SCM) with image acquisition at three delay time points (Figure 5).

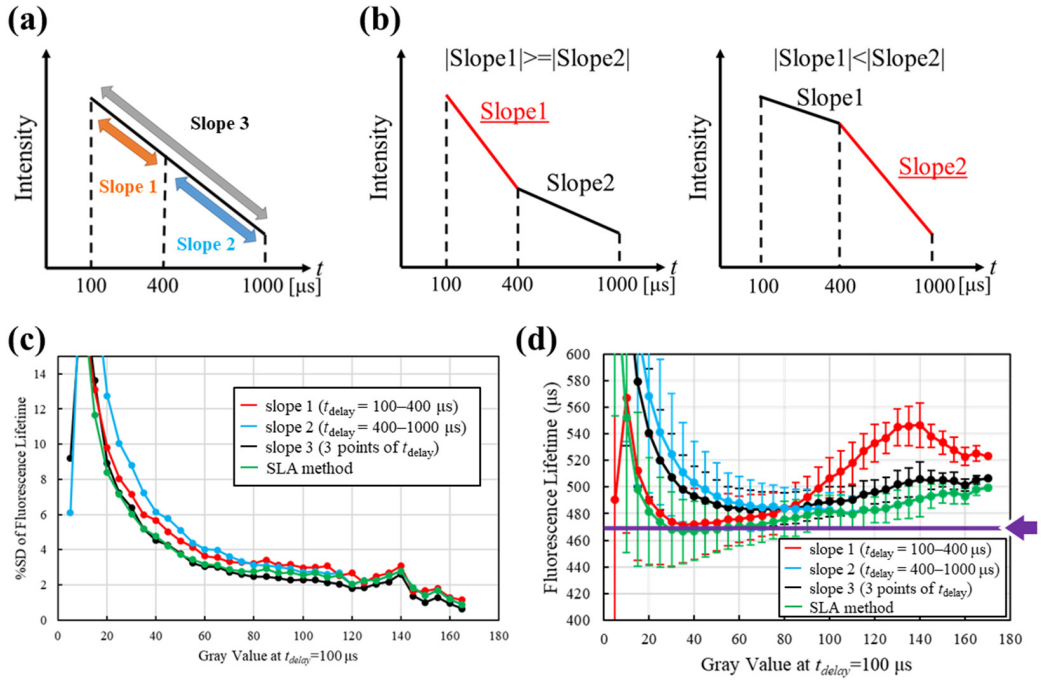

Figure 5. Calculation of the fluorescence lifetime by the proposed slope comparison method (SCM). (**a**) Slopes that can be used to calculate the lifetime based on data at three decay times. (**b**) Concept of selecting a delay time range (slope 1 or 2) for lifetime calculation from the two slopes in the SCM. At pixels that receive weak fluorescence, slope 1 becomes steeper than slope 2 because the data for slope 2 contains much noise. In this case, slope 1 is selected for lifetime calculation. At pixels that receive strong fluorescence, slope 2 becomes steeper than slope 1 owing to the partial saturation suggested in previous studies [23]. In this case, slope 2 is selected for lifetime calculation. (**c**) Deviation and (**d**) accuracy (relation to true value) of the fluorescence lifetime calculated from each slope in this NIRF-TGI experiment. An arrow presents the true value (470 µs) of the fluorescence lifetime of phosphor.

To investigate the performance of the SCM for lifetime calculation, the NIRF decay of $NaYF_4$: Nd^{3+}, Yb^{3+} (Yb^{3+}: $^2F_{5/2} \rightarrow {}^2F_{7/2}$) particles at 1000 nm with a known lifetime (470 µs, 25 °C) was observed with the NIRF-TGI under excitation with a pulsed laser at a wavelength of 808 nm. From the fluorescence images acquired at three delay times of 100, 400, and 1000 µs, the lifetime can be calculated using the slope obtained by the intensity ratio between 100 and 400 µs (slope 1), that obtained using the ratio between 400 and 1000 µs (slope 2), and that obtained using all three data points (slope 3) (Figure 5a).

The fluorescence lifetime was calculated by taking the inverse of the fluorescence intensity ratio (slope) observed at different delay times (t_{delay}). The three particular time points for the SCM were determined approximately based on the definition of fluorescence

lifetime as follows: (1) the time immediately after the complete disappearance of excitation light, (2) a time slightly shorter than the expected fluorescence lifetimes, and (3) a time of 2.5–3 times behind the second time point; while the optimal setting way for the three time points is a subject for future study. To ensure linearity between the light intensity and the signal observed at each pixel (grayscale) with a simple NIR camera, the following two points should be considered: (1) If the fluorescence is too weak, the signal-to-noise ratio will be low. (2) If the fluorescence is too strong, partial saturation will cause the grayscale to be lower than the true light level (and thus, the calculated fluorescence lifetime will be longer than the true value) [23]. Therefore, we devised the SCM to select the slope used to calculate the lifetime for each pixel according to the ratio of slope 1 to slope 2. In the SCM, the one with the larger absolute value of the slope between slopes 1 and 2 was used to calculate the fluorescence lifetime (Figure 5b). The fluorescence lifetime calculated by the SCM for NIRF-TGI showed a similar deviation (systematic error) to that obtained by using data from all imaging delay time points (3 points) (Figure 5c). However, the SCM exhibited the lowest inaccuracy (difference from the true value) (Figure 5d). Thus, the SCM can provide the most accurate results for fluorescence lifetime calculation, even when the number of delay time points to be imaged is reduced to shorten the total time of image acquisition.

4. Discussion

This study aimed to develop a lifetime-based multiplex 3D imaging method for NIRF in deep tissues by synchronizing an NIRF-TGI system [23] with a rotatable stage controlling the detection angles for NIRF-CT [26]. Lanthanide-doped ceramic nanoparticles were used as probes with different fluorescence lifetimes to be supplied for TGI. Nd^{3+} and Yb^{3+} were used as dopants to obtain emissions at 1000−1040 nm under 808 nm excitation. A multiplex scheme with two different lifetimes was provided by different host materials, $NaYF_4$ and YPO_4. We developed an SCM as an NIRF lifetime analysis method using conventional NIR cameras with reduced delay time points and demonstrated its effectiveness. While fluorescence lifetime-based tomography has been previously reported [15,33,34], the present study first reports in detail the relationship between the fluorescence decay at the projection plane, where images can be obtained directly with a detector (NIR camera), and the decay depicted on cross-sectional tomograms. Furthermore, the accuracy of the mapped fluorescence lifetimes on the tomograms is examined. Although we do not have preliminary NIRF-TGI-CT data of in vivo tissues, the availability of such NIR camera for in vivo NIRF-CT (not time-gated) of targets has been reported in mice [26]. Combining this with the time-gated technique, the NIRF-TGI-CT of this paper is expected to be applicable to in vivo samples. NIRF-CT results of fluorescence located in deep tissue in larger samples, which is observable with NIRF imaging, are affected by the refraction of fluorescence at the sample surface. However, this problem can be solved by immersing the sample in a liquid with a refractive index close to that of the sample [35]. The influence of light scattering by tissue samples, reported in NIRF-CT [36] and NIRF-TGI [23] imaging techniques, has not been examined in the present NIRF-TGI-CT, and is still an important issue of future work. The basic strategy of NIRF-TGI-CT is similar to that of MRI, that is, it depicts a cross-sectional image of the inside of a sample by contrasting the signal decay rate [37]. As with MRI, NIRF-TGI-CT currently requires more than ten minutes of the imaging time. However, the number of imaging angles and delay times can be modified according to the required accuracy for each case. Therefore, the imaging time can be shortened by reducing the number of images. The greatest advantage of the NIRF-TGI-CT method shown in this paper is to allow tomographic imaging of contrasts of the fluorescence lifetime of rare-earth phosphors (on the order of hundreds of microseconds), using a conventional NIR camera in combination with time-gated technique, instead of FLIM, which is commonly used to visualize the lifetime of molecular dyes (nanosecond order) with a high-speed camera. Although the time required for imaging using the NIRF-TGI-CT method is not as short as the FLIM method, the time-gated NIRF-CT for lifetime-based multiplex 3D imaging

technique presented in this study is expected to be applied to the acquisition of information on the deep interior of samples, especially biological tissues possessing refractive index interfaces that cause light scattering.

5. Conclusions

Three-dimensional (3D) multiplex fluorescence lifetimes were successfully depicted by developing a system combining the NIRF-TGI and CT techniques. Samples were subjected to an imaging system with a pulsed laser for excitation synchronized with triggers for the control of image acquisition and movement of the rotatable sample stage. In this system, two-dimensional projected images can be acquired from multiple angles at different delay times (several tens to hundreds of microseconds) after blocking the pulsed laser. CT via back-projection converted the intensity distribution information on the projected images into cross-sectional images at each delay time. The obtained images showed fluorescence decay on each pixel of the cross-sections. The fluorescence lifetime was determined as the decay rate and mapped onto the cross-sectional images; thus, the lifetimes of $NaYF_4$ and YPO_4 co-doped with Nd^{3+} and Yb^{3+} were well distinguished in the 3D image. By using fluorescence in NIR, the biologically transparent wavelength range, this imaging technique is applicable to 3D functional imaging, such as the temperature of targets in deep biological tissues.

Supplementary Materials: The following supporting information can be downloaded from https://www.mdpi.com/article/10.3390/app12157721/s1, Video S1: Three-dimensional image of fluorescence lifetimes of $NaYF_4$: Nd^{3+}, Yb^{3+} and YPO_4: Nd^{3+}, Yb^{3+} embedded in a column-shaped agar gel.

Author Contributions: Conceptualization, K.S. and M.U.; methodology, K.S., K.M., M.U. and K.O.; software, K.M.; analysis, investigation, and visualization, K.M. and M.U.; writing—original draft preparation, M.U. and K.M.; writing—review and editing, M.U., K.O. and K.S.; supervision, project administration, and funding acquisition, K.S. All authors have read and agreed to the published version of the manuscript.

Funding: This research was funded by the MEXT Grant-in-Aid for Scientific Research on Innovative Areas (Resonance Bio), no. 15H05950 and the MEXT Grant-in-Aid or Scientific Research (A), no. 19H01179.

Institutional Review Board Statement: Not applicable.

Informed Consent Statement: Not applicable.

Data Availability Statement: Data underlying the results presented in this paper may be obtained from the authors upon reasonable request.

Acknowledgments: We thank all the staff and graduate and undergraduate students of Soga Laboratory (Department of Materials Science and Technology, Tokyo University of Science), especially Takumi Chihara, Koki Nomura, Hikaru Haraguchi, and Hiroyuki Kurahashi for their technical assistance with phosphor synthesis.

Conflicts of Interest: The authors declare no conflict of interest.

References

1. Kwong, Y.; Mel, A.O.; Wheeler, G.; Troupis, J.M. Four-dimensional computed tomography (4DCT): A review of the current status and applications. *J. Med. Imaging Radiat. Oncol.* **2015**, *59*, 545–554. [CrossRef] [PubMed]
2. Beckh, S.; Bölcskei, P.L.; Lessnau, K.D. Real-time chest ultrasonography: A comprehensive review for the pulmonologist. *Chest* **2002**, *122*, 1759–1773. [CrossRef] [PubMed]
3. Yoo, J.; Lee, J.M.; Joo, I.; Lee, D.H.; Yoon, J.H.; Kang, H.J.; Ahn, S.J. Reproducibility of ultrasound attenuation imaging for the noninvasive evaluation of hepatic steatosis. *Ultrasonography* **2020**, *39*, 121–129. [CrossRef]
4. Andreasen, N.C. Evaluation of brain imaging techniques in mental illness. *Annu. Rev. Med.* **1988**, *39*, 335–345. [CrossRef] [PubMed]
5. Uz, Z.; Shen, L.; Milstein, D.M.J.; van Lienden, K.P.; Swijnenburg, R.-J.; Ince, C.; van Gulik, T.M. Intraoperative imaging techniques to visualize hepatic (micro)perfusion: An overview. *Eur. Surg. Res.* **2020**, *61*, 2–13. [CrossRef] [PubMed]

6. Smith, A.M.; Mancini, M.C.; Nie, S. Bioimaging: Second window for in vivo imaging. *Nat. Nanotechnol.* **2009**, *4*, 710–711. [CrossRef]
7. Anderson, R.R.; Parrish, J.A. The optics of human skin. *J. Investig. Dermatol.* **1981**, *77*, 13–19. [CrossRef] [PubMed]
8. Zako, T.; Yoshimoto, M.; Hyodo, H.; Kishimoto, H.; Ito, M.; Kaneko, K.; Soga, K.; Maeda, M. Cancer-targeted near infrared imaging using rare earth ion-doped ceramic nanoparticles. *Biomater. Sci.* **2015**, *3*, 59–64. [CrossRef]
9. *Transparency in Biology: Making Invisible Visible*; Soga, K.; Umezawa, M.; Okubo, K. (Eds.) Springer: Singapore, 2021.
10. Sato, D.; Takamatsu, T.; Umezawa, M.; Kitagawa, Y.; Maeda, K.; Hosokawa, N.; Okubo, K.; Kamimura, M.; Kadota, T.; Akimoto, T.; et al. Distinction of surgically resected gastrointestinal stromal tumor by near-infrared hyperspectral imaging. *Sci. Rep.* **2020**, *10*, 21852. [CrossRef] [PubMed]
11. Fan, Y.; Wang, P.; Lu, Y.; Wang, R.; Zhou, L.; Zheng, X.; Li, X.; Piper, J.A.; Zhang, F. Lifetime-engineered NIR-II nanoparticles unlock multiplexed in vivo imaging. *Nat. Nanotechnol.* **2018**, *13*, 941–946. [CrossRef]
12. Greger, K.; Neetz, M.J.; Reynaud, E.G.; Stelzer, E.H.K. Three-dimensional fluorescence lifetime imaging with a single plane illumination microscope provides an improved signal to noise ratio. *Opt. Express* **2011**, *19*, 20743–20750. [CrossRef] [PubMed]
13. Hirvonen, L.M.; Nedbal, J.; Almutairi, N.; Phillips, T.A.; Becker, W.; Conneely, T.; Milnes, J.; Cox, S.; Stürzenbaum, S.; Suhling, K. Lightsheet fluorescence lifetime imaging microscopy with wide-field time-correlated single photon counting. *J. Biophotonics* **2020**, *13*, e201960099. [CrossRef] [PubMed]
14. Yu, J.; Zhang, R.; Gao, Y.; Sheng, Z.; Gu, M.; Sun, Q.; Liao, J.; Wu, T.; Lin, Z.; Wu, P.; et al. Intravital confocal fluorescence lifetime imaging microscopy in the second near-infrared window. *Opt. Lett.* **2020**, *45*, 3305–3308. [CrossRef]
15. Zhang, L.; Gao, F.; He, H.; Zhao, H. Three-dimensional scheme for time-domain fluorescence molecular tomography based on Laplace transforms with noise-robust factors. *Opt. Exp.* **2008**, *16*, 7214–7223. [CrossRef] [PubMed]
16. Godavarty, A.; Sevick-Muraca, E.M.; Eppstein, M.J. Three-dimensional fluorescence lifetime tomography. *Med. Phys.* **2005**, *32*, 992–1000. [CrossRef]
17. McGinty, J.; Stuckey, D.W.; Soloviev, V.Y.; Laine, R.; Wylezinska-Arridge, M.; Wells, D.J.; Arridge, S.R.; French, P.M.W.; Hajnal, J.V.; Sardini, A. In vivo fluorescence lifetime tomography of a FRET probe expressed in mouse. *Biomed. Opt. Exp.* **2011**, *2*, 1907–1917. [CrossRef]
18. Xu, D.; Zhou, W.; Peng, L. Cellular resolution multiplexed FLIM tomography with dual-color Bessel beam. *Biomed. Opt. Exp.* **2017**, *8*, 570–578. [CrossRef]
19. Gu, L.; Hall, D.J.; Qin, Z.T.; Anglin, E.; Joo, J.; Mooney, D.J.; Howell, S.B.; Sailor, M.J. In vivo time-gated fluorescence imaging with biodegradable luminescent porous silicon nanoparticles. *Nat. Commun.* **2013**, *4*, 3326. [CrossRef] [PubMed]
20. Jin, D.; Pipper, J.A. Time-gated luminescence microscopy allowing direct visual inspection of lanthanide-stained microorganisms in background-free condition. *Anal. Chem.* **2011**, *83*, 2294–2300. [CrossRef] [PubMed]
21. Rice, W.L.; Shcherbakova, D.M.; Verkhusha, V.V.; Kumar, A.T.N. In Vivo tomographic imaging of deep-seated cancer using fluorescence lifetime contrast. *Cancer Res.* **2015**, *75*, 1236–1243. [CrossRef]
22. Del Rosal, B.; Ortgies, D.H.; Fernández, N.; Sanz-Rodríguez, F.; Jaque, D.; Rodríguez, E.M. Overcoming autofluorescence: Long-lifetime infrared nanoparticles for time-gated in vivo imaging. *Adv. Mater.* **2016**, *28*, 10188–10193. [CrossRef] [PubMed]
23. Chihara, T.; Umezawa, M.; Miyata, K.; Sekiyama, S.; Hosokawa, N.; Okubo, K.; Kamimura, M.; Soga, K. Biological deep temperature imaging with fluorescence lifetime of rare-earth-doped ceramics particles in the second NIR biological window. *Sci. Rep.* **2019**, *9*, 12806. [CrossRef] [PubMed]
24. Zacharakis, G.; Kambara, H.; Shih, H.; Ripoll, J.; Grimm, J.; Saeki, Y.; Weissleder, R.; Ntziachristos, V. Volumetric tomography of fluorescent proteinsthrough small animalsin vivo. *Proc. Natl. Acad. Sci. USA* **2005**, *102*, 18252–18257. [CrossRef]
25. Stuker, F.; Ripoll, J.; Rudin, M. Fluorescence molecular tomography: Principles and potential for pharmaceutical research. *Pharmaceutics* **2011**, *3*, 229–274. [CrossRef]
26. Umezawa, M.; Sera, T.; Yokota, H.; Takematsu, M.; Morita, M.; Yeroslavsky, G.; Kamimura, M.; Soga, K. Computed tomography for in vivo deep over-1000 nm near-infrared fluorescence imaging. *J. Biophotonics* **2020**, *13*, e202000071. [CrossRef] [PubMed]
27. Haro-González, P.; Martínez-Maestro, L.; Martín, I.R.; García-Solé, J.; Jaque, D. High-sensitivity fluorescence lifetime thermal sensing based on CdTe quantum dots. *Small* **2012**, *8*, 2652–2658. [CrossRef] [PubMed]
28. Kamimura, M.; Saito, R.; Hyodo, H.; Tsuji, K.; Umeda, I.O.; Fujii, H.; Soga, K. Over-1000 nm near-infrared fluorescence and SPECT/CT dual-modal in gigo imaging based on rare-earth doped ceramic nanophosphors. *J. Photopolym. Sci. Technol.* **2016**, *29*, 525–532. [CrossRef]
29. Powell, R.C. *Physics of Solid-State Laser Materials*; Springer: New York, NY, USA, 1998.
30. Ortgies, D.H.; Tan, M.; Ximendes, E.C.; Del Rosal, B.; Hu, J.; Xu, L.; Wang, X.; Martín Rodríguez, E.; Jacinto, C.; Fernandez, N.; et al. Lifetime-encoded infrared-emitting nanoparticles for in vivo multiplexed imaging. *ACS Nano* **2018**, *12*, 4362–4368. [CrossRef] [PubMed]
31. Parchur, A.K.; Prasad, A.I.; Rai, S.B.; Tewari, R.; Sahu, R.K.; Okram, G.S.; Singh, R.A.; Ninhthoujam, R.S. Observation of intermediate bands in Eu^{3+} doped YPO_4 host: Li^+ ion effect and blue to pink light emitter. *AIP Adv.* **2012**, *2*, 032119. [CrossRef]
32. Suyver, J.F.; Grimm, J.; van Veen, M.K.; Biner, D.; Krämer, K.W.; Güdel, H.U. Upconversion spectroscopy and properties of $NaYF_4$ doped with Er^{3+}, Tm^{3+} and/or Yb^{3+}. *J. Lumin.* **2006**, *117*, 1–12. [CrossRef]
33. McGinty, J.; Tahir, K.B.; Laine, R.; Talbot, C.B.; Dunsby, C.; Neil, M.A.A.; Quintana, L.; Swoger, J.; Sharpe, J.; French, P.M.W. Fluorescence lifetime optical projection tomography. *J. Biophotonics* **2008**, *1*, 390–394. [CrossRef] [PubMed]

34. McGinty, J.; Taylor, H.B.; Chen, L.; Bugeon, L.; Lamb, J.R.; Dallman, M.J.; French, P.M.W. In Vivo fluorescence lifetime optical projection tomography. *Biomed. Opt. Exp.* **2011**, *2*, 1340–1350. [CrossRef] [PubMed]
35. Takematsu, M.; Umezawa, M.; Sera, T.; Kitagawa, Y.; Kurahashi, H.; Yamada, S.; Okubo, K.; Kamimura, M.; Yokota, H.; Soga, K. Influence of the difference in refractive index on the interface of an object and the surrounding in near-infrared fluorescence tomography. *Appl. Opt.* **2022**, *61*, 638–644. [CrossRef] [PubMed]
36. Barber, W.C.; Lin, Y.; Nalcioglu, O.; Iwanczyk, J.S.; Hartsough, N.R.; Gulsen, G. Combined fluorescence and X-ray tomography for quantitative in vivo detection of fluorophore. *Technol. Cancer Res. Treat.* **2010**, *9*, 45–52. [CrossRef] [PubMed]
37. Mori, S.; Barker, P.B. Diffusion magnetic resonance imaging: Its principle and applications. *Anat. Rec.* **1999**, *257*, 102–109. [CrossRef]